33RD CONGRESS
OF THE INTERNATIONAL COUNCIL
OF THE AERONAUTICAL SCIENCES
STOCKHOLM, SWEDEN, 4–9 SEPTEMBER, 2022

ICAS
2022
SWEDEN

THE IMPACT OF REACTION MECHANISM COMPLEXITY IN LES MODELING OF LIQUID KEROSENE SPRAY COMBUSTION

Arvid Åkerblom

Lund University, Dept. of Energy Sciences, Div. of Heat Transfer, Lund, PO Box 118, SE 221-00, Sweden

Abstract

Large Eddy Simulation (LES) is a powerful tool for studying turbulent combustion, but its computational cost necessitates that any combustion models used in conjunction must be compact as well as accurate. A suitable balance between cost and accuracy may be found in the use of finite-rate pathway-centric reaction mechanisms, but these can vary greatly in cost and accuracy depending on the number of species and reactions involved. In this study, the impact of mechanism complexity is studied so that appropriate mechanisms can be chosen for future LES studies, and to aid in the development of new LES-optimized reaction mechanisms. LES is performed on a generic gas turbine combustor operating at two sets of typical aeroengine conditions. The liquid fuel spray is modeled using Lagrangian particle tracking. Two pathway-centric reaction mechanisms for the kerosene surrogate $C_{12}H_{23}$ are employed, resulting in four cases. One mechanism is more complex, as well as three times more computationally expensive, than the other. The mechanisms show similar results with regard to large-scale flame dynamics, but major product mass fractions in the emissions differ by $\sim 4\%$ and $< 1\%$ at idle and cruise conditions, respectively. The equilibrium OH concentration predicted by the more complex mechanism is ~ 2 and ~ 8 times greater than that of the simpler mechanism at idle and cruise conditions, respectively. The more complex mechanism predicts more heat release at the inner shear layer, while the simpler mechanism predicts a mostly quenched flame there.

Keywords: Gas turbine combustor; Computational fluid dynamics; Spray combustion; Large-eddy simulation; Finite-rate chemistry

1. Introduction

Kerosene-fueled jet engines are ubiquitous in modern aircraft. In the development of the next generation of jet engines, key areas of research are efficiency improvements, emission reduction, enhanced compatibility with new and existing aviation biofuels, and avoiding damaging thermoacoustic instabilities. Due to the relative wealth of data pertaining to conventional kerosene-based jet fuels compared to sustainable biofuels, simulation studies of biofuels should be preceded by a thorough validation study using conventional fuels. Such validation studies also provide results that can later be compared with equivalent results from biofuels. With the growing capabilities of supercomputers, ever more sophisticated computational tools can be employed to study the internal combustion processes of jet engines and provide key insights that are difficult to obtain from physical experiments. One such tool is Large Eddy Simulation (LES), a turbulence modeling method within Computational Fluid Dynamics (CFD) that allows the large-scale motions of turbulent combustion to be resolved in time and space, while the influence of smaller and more isotropic motions is modeled. This provides a more expensive, but potentially more accurate and reliable, picture of turbulence than can be attained with Reynolds-Averaged Navier-Stokes (RANS) methods.

Due to the high computational cost of LES and detailed chemistry models, chemical reaction mechanisms employed for finite-rate chemistry in LES must be compact yet accurate. Such reduced mechanisms are naturally based on simplifications and approximations which may give rise to less

comprehensive results. The impact of reaction mechanism complexity on LES should therefore be gauged for various cases, so that appropriate mechanisms can be chosen for future studies and new mechanisms, optimized for LES, can be developed.

In this study, turbulent spray combustion inside a generic kerosene-fueled single-cup combustor is studied with LES and finite-rate chemistry modeling, with Lagrangian particle tracking for the liquid spray. The same case has been studied experimentally by DLR, [1] [2], and numerically by Jones et al., [3]. Two sets of operating conditions are used, emulating an aeroengine at idle and cruise conditions, respectively. Two pathway-centric chemical reaction mechanisms, one large (henceforth labeled A3), [4] [5], and one small (henceforth labeled Z77), [6], are used to model the combustion process. In both of these mechanisms, the fuel is modeled as a single chemical species with the formula $C_{12}H_{23}$. (This specific formula is considered by [4] [5] to be most appropriate for modeling JP-5 fuel, while $C_{11}H_{22}$ is more appropriate for Jet A.) The results from the mechanisms are compared, and their differences related to the underlying characteristics of each mechanism. Presented results include heat release, temperature, and key species concentrations. A visual comparison with experimental results is made to ensure that the results are reasonable, but the primary aim is to gauge the difference between the predictions of the two mechanisms.

2. Methodology

The simulation case is based on an experimental combustor, [1], at DLR Institute of Propulsion Technology. It has a square cross section of 102 x 102 mm^2 and a length of 264 mm. The single burner uses prefilming air-blast atomization to create a liquid fuel spray. The combustor has been operated at idle conditions, corresponding to inlet temperatures and pressures of 550 K and 4 bar, as well as cruise conditions, corresponding to 650 K and 10 bar, [2]. A global equivalence ratio of 0.74 (neglecting air flow from window cooling film) was used at both sets of conditions.
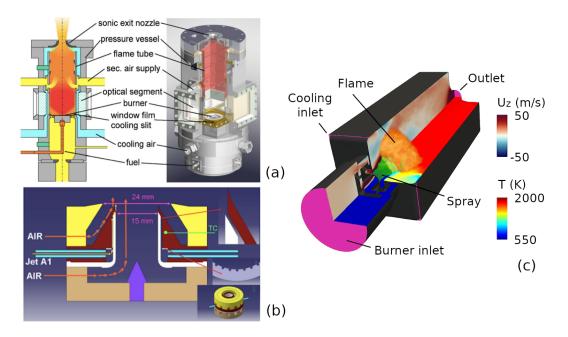

Figure 1 – (a) Schematic of the combustor. (b) Schematic of the burner. (c) Overview of the simulation domain with boundaries, spray, and flame, as well as color plots of mean axial velocity and temperature.

A typical Eulerian LES model is used for the gas phase, based on implicitly filtered transport equations for mass (Eq. 1a), momentum (1b), energy (1c), and species concentrations (1d). The specific formulation of the equations is explained in more detail by Fedina, [7]. Source terms with the subscript "l" describe liquid-gas interactions while "c" denotes combustion chemistry. The symbol $\tilde{H}_K$ is used for compact notation and represents the sum of filtered enthalpy, filtered kinetic energy, and subgrid

kinetic energy: $\tilde{H}_K = \tilde{h} + \frac{1}{2}|\tilde{\mathbf{v}}|^2 + k$. The equations are closed by assuming Fickian diffusion, Fourier heat conduction, and ideal gas conditions, [8]. The viscosity is calculated using Sutherland's law with constant Prandtl and Schmidt numbers, [9]. Source terms originating from unresolved phenomena are modeled using subgrid kinetic energy, which is obtained from the one-equation subgrid kinetic energy model with constant coefficients, [10]. A variant of the Partially Stirred Reactor model, [11], which provides local estimates for the amount of fine structures within the flame at subgrid scales, is used to calculate the filtered chemical source terms.

$$\frac{\partial \overline{\rho}}{\partial t} + \nabla \cdot (\overline{\rho}\tilde{\mathbf{v}}) = \bar{\dot{\rho}}_l \tag{1a}$$

$$\frac{\partial \overline{\rho}\tilde{\mathbf{v}}}{\partial t} + \nabla \cdot (\overline{\rho}\tilde{\mathbf{v}} \otimes \tilde{\mathbf{v}}) = -\nabla \overline{p} + \nabla \cdot \left(2\overline{\mu}\tilde{\mathbf{D}} - \frac{2}{3}\overline{\mu}(\nabla \cdot \tilde{\mathbf{v}})\mathbf{I}\right) + \overline{\mathbf{f}}_l - \nabla \cdot \mathbf{B} \tag{1b}$$

$$\frac{\partial \overline{\rho}\tilde{H}_K}{\partial t} + \nabla \cdot (\overline{\rho}\tilde{H}_K\tilde{\mathbf{v}}) = \frac{\partial \overline{p}}{\partial t} + \left(2\overline{\mu}\tilde{\mathbf{D}} - \frac{2}{3}\overline{\mu}(\nabla \cdot \tilde{\mathbf{v}})\mathbf{I}\right) \cdot \nabla \tilde{\mathbf{v}} + \nabla \cdot (\overline{\alpha}\nabla\tilde{h}) + \bar{\dot{q}}_c + \bar{\dot{q}}_l - \nabla \cdot \mathbf{b_E} \tag{1c}$$

$$\frac{\partial \overline{\rho}\tilde{Y}_i}{\partial t} + \nabla \cdot (\overline{\rho}\tilde{Y}_i\tilde{\mathbf{v}}) = \nabla \cdot (D_i\nabla\tilde{Y}_i) + \bar{\dot{\omega}}_{ic} + \overline{\dot{m}}_{il} - \nabla \cdot \mathbf{b_i} \tag{1d}$$

Fuel is injected along the circumference of the prefilmer lip, as shown in Figure 1. The fuel should in reality form a rapidly atomizing liquid film on the lip, [2], but is here considered fully dispersed at injection. The liquid phase is modeled as a cloud of Lagrangian particles, each representing a group of spherical droplets with identical properties. The Eulerian and Lagrangian phases are four-way coupled, meaning that they influence each other while individual particles may also interact upon collision according to a trajectory model, [12]. Secondary droplet breakup is described by the Reitz-Diwakar model, [13]. The Lagrangian phase loses momentum to the Eulerian phase through the drag force (as experienced by a solid sphere), while heat is transferred between the phases according to the Ranz-Marshall model, [14]. Evaporation and boiling are modelled using the approach of Zuo et al, [15]. Mathematically, these phase interactions constitute source terms within the governing equations of each phase.

A block-structured hexahedral grid composed of 6.0 million cells is used to resolve the gas phase, and Lagrangian particles are injected at a rate of 10^9/s. All model equations are solved using a finite-volume code based on the OpenFOAM library, [16]. All simulations are run for 38 ms to establish a statistically steady state, after which data is collected over the course of 11 ms. In order to gauge the mesh resolution sensitivity, data is also collected for 5 ms using a finer mesh produced by splitting each hexahedron into eight similar hexahedra, resulting in 48 million cells. Due to to the significantly higher cost that accompanies the increase in mesh resolution, an inexpensive two-step global reaction mechanism based on [17] is employed for this comparison. Using the finer mesh results in a 0.85% increase in the total time-averaged heat release when compared to the base mesh, a difference small enough to justify the use of the base mesh.

The two employed reaction mechanisms are designed for kerosene-based jet fuel and consider it to be a single species with the model chemical formula $C_{12}H_{23}$ (when the number of hydrogen atoms in the fuel species may only be an integer). Z77 contains 33 species and 77 reactions, while A3 contains 50 species and 277 reactions. Particular attention was given to pyrolysis (fuel breakdown) in the development of A3. In the LES simulations of the present work, A3 requires roughly three times the total simulation time of Z77 at equivalent Courant numbers. Figure 2 shows some of the key parameters of the mechanisms: laminar flame speed (s_u), maximum flame temperature (T_{max}), ignition delay time (τ_{ign}), and non-premixed extinction strain rate (σ_{ext}). These parameters are computed using 0D (τ_{ign}) and 1D (s_u, T_{max}, σ_{ext}) simulations in Ansys Chemkin-Pro, [18]. Extinction strain rates are computed for a non-premixed counterflow flame fed by a fuel/nitrogen mixture ($T = 473$ K) on one side and a pure oxygen ($T = 300$ K) stream on the other. The s_u and T_{max} results come from the same set of simulations, where a laminar flame propagates into an unburnt fuel mixture at $T = 470$ K. The s_u, T_{max}, and τ_{ign} panels contain two sets of graphs, corresponding to low (dashed lines) and high (solid lines) pressure. Experimentally measured values are included for n-dodecane and Jet A,

as well as POSF10289, a test fuel closely approximating JP-5, [4] [5]. Following the approach of [19], the results marked by diamonds have been scaled by $(T_1/T_0)^{1.83}$ to match the conditions of the other results in the same panel.

Figure 2 shows that both mechanisms have similar kinetics, though Z77 has a somewhat higher flame speed, hotter flame, and slower ignition. A comparison with experimental results seems to indicate that A3 is more realistic than Z77 as it follows the POSF10289 measurements very closely, but this is mainly because those specific experimental results were used to validate A3. With this bias in mind, both mechanisms show good agreement with experimentally measured values for typical kerosene-based aviation fuels. Both mechanisms capture the Negative Temperature Coefficient (NTC) effect, where relatively fast ignition can occur at low temperatures. This effect is more pronounced in Z77 than in A3. The mechanisms display similar σ_{ext} in dilute mixtures ($m_{fuel}/m_{N2} < 0.075$) but diverge at more fuel-rich mixtures. At $m_{fuel}/m_{N2} = 0.1$, A3 tolerates 37% higher strain rates than Z77 without undergoing extinction. Both mechanism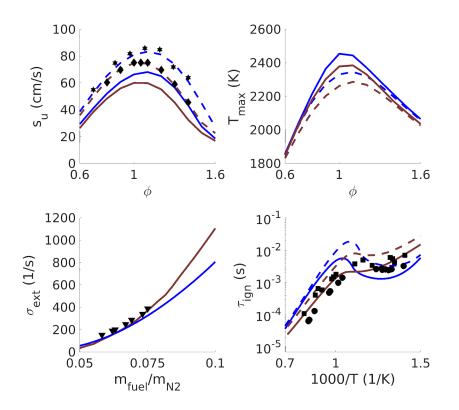s are about equal in pressure sensitivity with regard to s_u and T_{max}, while A3 is more pressure-sensitive than Z77 at high temperatures with regard to τ_{ign}.

Figure 2 – Kinetics of both reaction mechanisms. Clockwise, from top left: s_u (1 and 2.5 atm), T (1 and 2.5 atm), τ_{ign} (10 and 20 atm), σ_{ext} (1 atm). Solid lines: high pressure. Dashed lines: low pressure. (—): A3. (—): Z77. Experimental measurements: (✷): Kumar et al. (1 atm), Jet A, [20]. (◆): Wang et al. (1 atm), POSF10289, [5]. (▼): Liu et al. (1 atm), n-dodecane, [21]. (■): Vasu et al. (20 atm), Jet A, [22]. (●): Wang et al. (12 atm), POSF10289, [5].

3. Results

Figure 3 shows the dynamic behavior of the spray and flame at both idle and cruise conditions. Each spray parcel is rendered as a sphere colored by temperature, showing a rapid heat-up to boiling temperature after injection. A green region can be seen near the hotter parts of the spray, indicating a high concentration of evaporated fuel. A thin layer of formyl radical (HCO) covers the outside of the fuel cloud. As HCO is a very short-lived radical, the HCO layer indicates the presence of a flame front. Downstream of the flame front, a postflame zone containing high concentrations of the hydroxyl radical (OH) fades into the chemical equilibrium zone where carbon dioxide (CO_2) dominates over the other mentioned species. A magenta-colored pressure iso-surface shows a helical region of low

pressure, which forms as the 'eye' of the swirling flow downstream of the burner precesses around the central axis. Such a structure is referred to as a Precessing Vortex Core (PVC).

It can be plainly seen in Figure 3 that all stages of combustion occur significantly faster at cruise conditions than idle conditions; the spray and flame are much more compact and close to the burner despite a higher mass flow rate. The primary cause of this difference in turbulent flame speed is the significantly stronger mixing of the fuel with the hot exhaust gases at cruise conditions, which is in part due to the higher Reynolds number and thus stronger turbulent fluctuations, but also due to self-excited longitudinal acoustic waves, with an amplitude of 4.8% (Z77) and 4.3% (A3) of the mean pressure, causing periodic velocity oscillations. The same acoustic mode is excited at idle conditions as well, though only with an amplitude of 0.61% (Z77) and 0.34% (A3) of the mean pressure. The relatively high flame lift at idle conditions provides the PVC with ample space to induce helical motions in the spray and flame, which consequently also give rise to azimuthal pressure waves with an amplitude of 0.18% (Z77) and 0.36% (A3) of the mean pressure.

Figure 4 shows volume renderings of both instantaneous and time-averaged temperature in each simulation. Due to the strong mixing at cruise conditions, the Outer Recirculation Zone (ORZ) is much more well-mixed with the hot downstream region than at idle conditions.
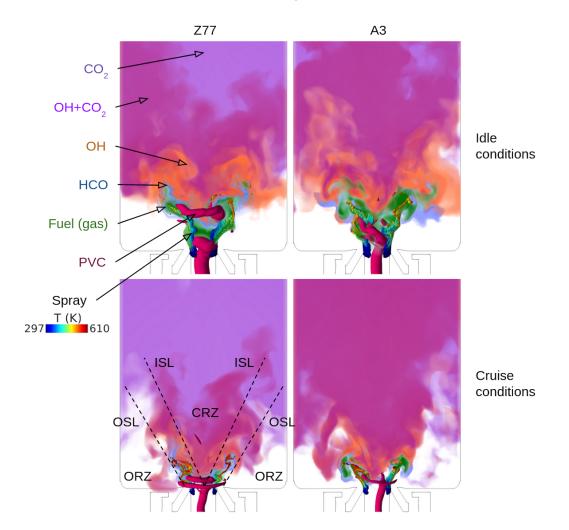

Figure 3 – Overview of the combustion process. Left to right: Z77, A3. Top to bottom: idle conditions, cruise conditions. High gaseous concentrations of four different species are represented by volume renderings of different color. The darker shade of purple indicates relatively high concentrations of both OH and CO_2. A magenta-colored pressure iso-surface shows the location of the PVC. PVC = Precessing Vortex Core. CRZ = Central Recirculation Zone. ISL = Inner Shear Layer. OSL = Outer Shear Layer. ORZ = Outer Recirculation Zone. Lagrangian particles are not to scale.
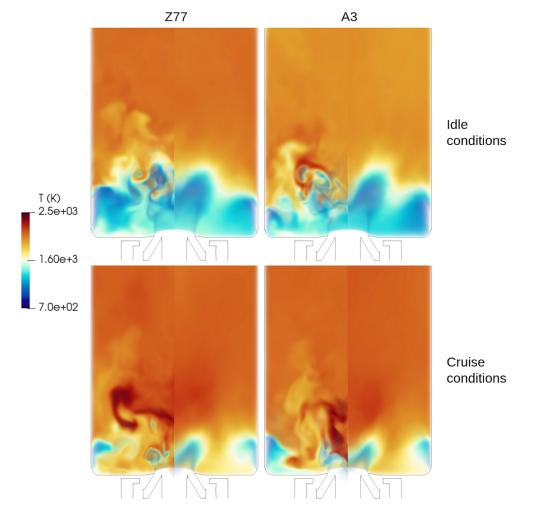
Figure 4 – Volume rendering of temperature in each simulation. Left to right: Z77, A3. Top to bottom: idle conditions, cruise conditions. In each panel, left to right: instantaneous temperature, time-averaged temperature.

A detailed view of the global combustion process is presented in Figure 5, where planarly and temporally averaged mass fractions of some key species are plotted along the axial direction through the first 100 mm of the combustion chamber. The temperature is included as well. The difference in turbulent flame speed is once again visible as the products water (H_2O) and carbon dioxide (CO_2) reach asymptotic levels much sooner at cruise conditions than at idle conditions. The two mechanisms produce quite similar emission profiles overall, with a number of differences (most notably the concentrations of the formyl and hydroxyl radicals HCO and OH) which are now discussed.

The peak fuel mass fraction is $\sim 5\%$ higher for A3 than for Z77, at both idle and cruise conditions. This is likely because the different pyrolysis pathways employed by the mechanisms produce slightly different breakdown rates for the fuel surrogate species. Z77 produces roughly twice as much formyl radical as A3, which is likely because A3, as a reaction mechanism, contains more short-lived radicals which tend to occupy the same space. When the chemical behavior of the near-flame region is of interest, a complex reaction mechanism evidently provides a more detailed picture than a simple one. The hydroxyl radical appears in much higher density than the formyl radical, which means that the magnitude of its concentration is much more similar between the mechanisms. Both mechanisms predict a stable equilibrium concentration far downstream of the flame, but the predictions of its magnitude are quite different. A3 predicts a higher OH mass fraction than Z77, by a factor of ~ 2 at idle conditions and ~ 8 at cruise conditions. There is clearly some crucial difference between the mechanisms in their treatment of the formation and consumption of the hydroxyl radical, and the size of the discrepancy depends heavily on operating conditions.

6

At idle conditions, the asymptotic water and carbon dioxide mass fractions are $\sim 4\%$ higher for Z77 when compared to A3. Z77 also produces an asymptotic temperature about 50 K higher than that of A3, which corresponds to a 3% difference relative to a reference temperature of 298.15 K. These differences imply that combustion is overall more complete for Z77 than for A3 in the region downstream of the flame. The mechanisms behave much more similarly at cruise conditions, with major product mass fractions and temperature very slightly ($< 1\%$) higher for A3 than for Z77. The flow-through time in the combustor and the mixing rate between the fuel and oxidizer are faster at cruise conditions, which means that converged time averages may be collected over shorter periods of time. A longer data collection period at idle conditions may shrink the gap between the results produced by the two mechanisms, and will be employed in subsequent studies. However, the 1D simulation results presented in Figure 2 suggest that A3 should still produce a lower temperature, and that this difference should be more pronounced at low pressure (idle conditions) than at high pressure (cruise conditions).
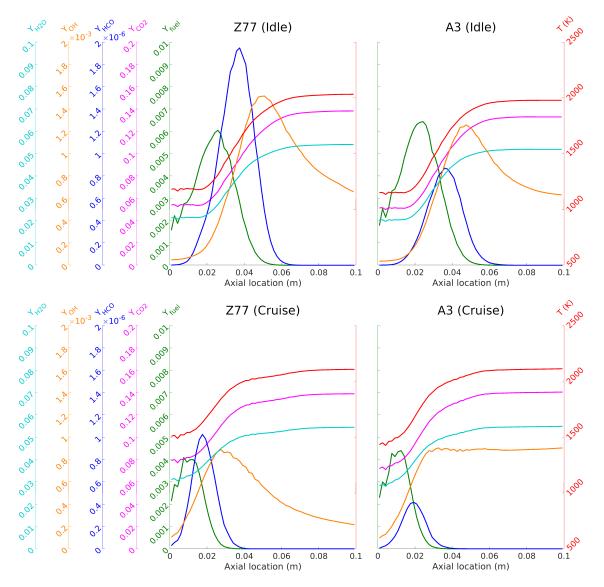

Figure 5 – Planarly and temporally averaged mass fractions of five important species as well as temperature, along the axial direction in the region just downstream of the burner. Left to right: Z77, A3. Top to bottom: idle conditions, cruise conditions.

Figure 6 contains time-averaged, azimuthally integrated color plots of the chemical heat release in each simulation, which provide a picture of the mean shape and location of the flame. The results are normalized separately for each mechanism by the highest value observed at cruise conditions. Experimentally measured OH chemiluminescence, [2], which indicates high levels of heat release, is included as well. Qualitatively, the simulation results match the experimental data quite well, though more so at cruise conditions. The flame lift and fuel penetration depth are overpredicted at idle conditions. Ongoing investigations with other reaction mechanisms suggest that the choice of fuel surrogate, here $C_{12}H_{23}$, has a significant impact on flame shape at idle conditions; better agreement may be achieved by using $C_{11}H_{22}$, which is considered by [4] [5] to better represent typical Jet A. The two mechanisms produce very similar flames, with much of the chemical activity occurring at the Inner Shear Layer (ISL) and within the primary flow cone between the recirculation regions. No heat is released at the Outer Shear Layer (OSL) because there is little to no fuel present there. The fact that both mechanisms produce flames of such similar shape despite their differences with regard to s_u, τ_{ign}, T_{max}, and σ_{ext} (see Figure 2), suggests that these parameters, and by extension the detailed kinetics of the mechanisms, has a relatively small effect on the mean flame shape in this case. Instead, the turbulent and thermoacoustic mixing between burnt and unburnt gas dictates where the fuel and air concentrations roughly correspond to the stoichiometric mixture fraction (which depends on the choice of fuel surrogate), and thus where the flame front is located, [23].
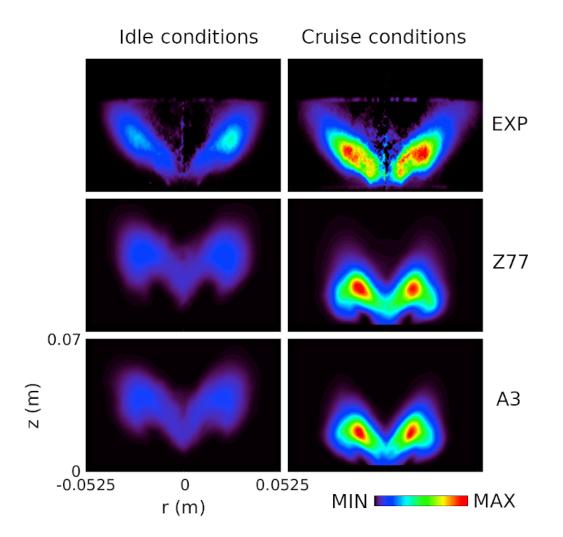

Figure 6 – Top row: experimentally measured mean OH chemiluminescence, an indicator of heat release. Experimental figures taken from Meier et al, [2]. Remaining rows: Time-averaged, azimuthally integrated combustion heat release in all simulations. Left to right: idle conditions, cruise conditions.

Figure 7 was produced in the same way as Figure 6, but shows the OH mass fraction instead. In this case, the simulation results are normalized by the highest number observed at idle conditions, which is slightly higher than that seen at cruise conditions. The included experimental results, [2], are in fact color plots of the temperature, not the OH concentration itself. Because the temperature was inferred from OH-PLIF measurements, however, the color plots also provide the shape of the OH distribution. As with the heat release in Figure 6, the OH distributions in Figure 7 capture the overall shape of the experimental results, though the flame lift is overpredicted at idle conditions. Comparing the heat release and the OH distributions, it seems that the highest concentration of OH is found in regions with high heat release. This is the hot region where OH is initially produced by fuel oxidation. The concentration quickly decreases downstream, as additional reactions convert OH to other radicals as well as the stable product H_2O. The OH distributions predicted by the two mechanisms are markedly different. As previously seen in Figure 5, OH is more plentiful outside the main heat release zone for A3 than for Z77. This can also be seen in Figure 7 where A3 displays a significantly wider distribution, especially at cruise conditions. Furthermore, Z77 shows peak concentrations located mainly between the inner and outer shear layers, while A3 shows peak concentrations all along the inner shear layer as well.
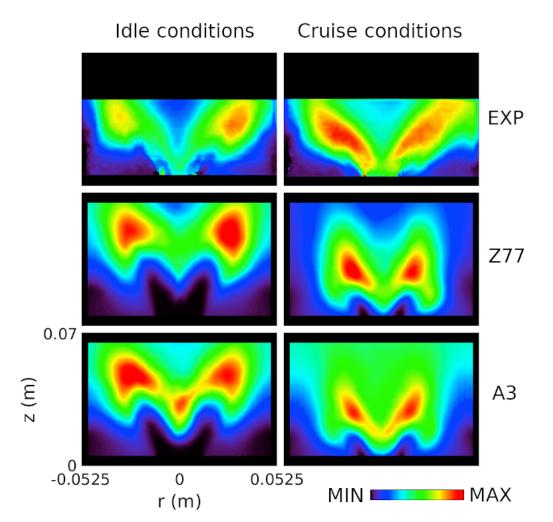

Figure 7 – Top row: experimentally measured mean temperature, based on OH-PLIF measurements. Experimental figures taken from Meier et al, [2]. Remaining rows: Time-averaged, azimuthally integrated OH mass fraction in all simulations. Left to right: idle conditions, cruise conditions.

Figure 8 provides a picture of the relationship between heat release and turbulence in each of the simulated flames. In a box-shaped region surrounding the flame, cells are sorted into bins based on the mean magnitude of local velocity fluctuations, defined as $\sqrt{u'^2 + v'^2 + w'^2}$ where u'^2, v'^2, and w'^2 are the variances of the three velocity components. The total heat release in each such bin is then computed and divided by the bin resolution, producing distributions of heat release in velocity fluctuation space. The integral of each curve is thereby made equal to the total mean heat release in the corresponding flame. The quality of the data clearly degrades as each curve approaches its maximum velocity fluctuation, as the number of cells in each bin becomes progressively fewer. Bins with fewer than 10 cells are omitted. At idle conditions, A3 predicts significantly higher heat release than Z77 in regions with fluctuations larger than 40 m/s. This is because A3 gives a high degree of chemical activity at the strongly turbulent ISL, while Z77 predicts a relatively quenched flame there. This lower tolerance of turbulence may be linked to the generally lower extinction strain rates σ_{ext} of Z77, shown in Figure 2. Further studies, employing a wider range of reaction mechanisms, are required in order to establish a potential correlation between σ_{ext} and local quenching in LES. If such a correlation is found, σ_{ext} may prove to be a useful parameter for predicting and characterizing the behavior of fuels and the mechanisms that are used to model them. The mechanisms behave more similarly at cruise conditions, making it difficult to extract constructive information from the lower panel of Figure 8.
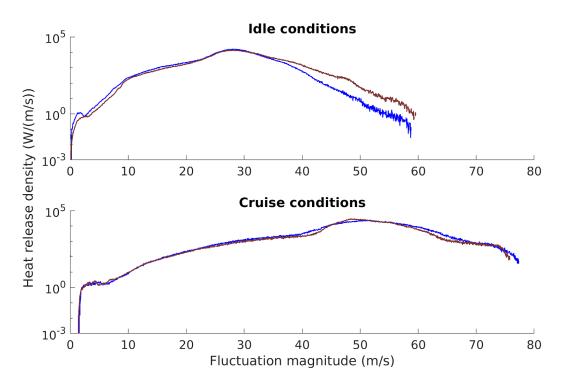

Figure 8 – Mean heat release in regions of different turbulent intensity. (——): A3. (——): Z77.

4. Conclusion

Spray combustion in a generic single-cup combustor has been modeled using LES and two chemical reaction mechanisms in order to gauge the difference between them. The conclusions are summarized below.

- Both mechanisms predict the same overall flame dynamics, with a high flame lift and a strong precessing vortex core at idle conditions, and a compact flame with strong thermoacoustic fluctuations at cruise conditions.

- At idle conditions, the simpler mechanism (Z77) predicts $\sim 4\%$ higher CO_2 and H_2O mass fractions and a $\sim 3\%$ higher temperature in the emissions, compared to the more complex mechanism (A3). These differences amount to $< 1\%$ at cruise conditions.

- While the simpler mechanism (Z77) predicts high OH concentrations in the near-flame region and low concentrations elsewhere, the more complex mechanism (A3) predicts a more even distribution as well as a significantly higher equilibrium concentration; ~ 2 times higher at idle conditions, and ~ 8 times higher at cruise conditions.

- The more complex mechanism (A3) predicts a large amount of heat release at the inner shear layer, while the simpler mechanism predicts a mostly quenched flame there. This difference may be explained by the fact that the former has an overall higher extinction strain rate, but further simulation studies are needed in order to establish whether such a correlation exists.

5. Acknowledgements

6. Contact Author Email Address

arvid.akerblom@energy.lth.se

7. Copyright Statement

References

[1] T. Behrendt, M. Frodermann, C. Hassa, J. Heinze, B. Lehmann, and K. Stursberg. Optical Measurements of Spray Combustion in a Single Sector Combustor from a Practical Fuel Injector at Higher Pressures. In *Symp. on Gas Turbine Engine Combustion, Emissions and Alternative Fuels*, Lisboa, 1999.

[2] U. Meier, J. Heinze, S. Freitag, and C. Hassa. Spray and Flame Structure of a Generic Injector at Aeroengine Conditions. *J. Eng. For Gas Turbines and Power*, 134(3):031503, 2012.

[3] W. P. Jones, A. J. Marquis, and K. Vogiatzaki. Large-eddy simulation of spray combustion in a gas turbine combustor. *Combust. Flame*, 161:222–239, 2014.

[4] H. Wang, R. Xu, K. Wang, et al. A physics-based approach to modeling real-fuel combustion chemistry - I. Evidence from experiments, and thermodynamic, chemical kinetic and statistical considerations. *Combust. Flame*, 193:502–519, 2018.

[5] R. Xu, K. Wang, S. Banerjee, et al. A physics-based approach to modeling real-fuel combustion chemistry – II. Reaction kinetic models of jet and rocket fuels. *Combust. Flame*, 193:520–537, 2018.

[6] N. Zettervall, C. Fureby, and E. J. K. Nilsson. A reduced chemical kinetic reaction mechanism for kerosene-air combustion. *Fuel*, 269:117446, 2020.

[7] B. Fedina. *Post-Detonation Afterburning of High Explosives*. PhD thesis, Department of Energy Sciences, Lund University, Lund, 2017.

[8] S. Menon and C. Fureby. In R. Blockley and W. Shyy, editors, *Encyclopedia of Aerospace Engineering*. John Wiley and Sons, 2010.

[9] E. Giacomazzi, F. R. Picchia, and N. Arcidiacono. On the Distribution of Lewis and Schmidt Numbers in Turbulent Flames. In *30th Meeting on Combustion, Italian Section*. Ischia, 2007.

[10] A. Yoshizawa and K. Horiuti. A Statistically-Derived Subgrid-Scale Kinetic Energy Model for the Large-Eddy Simulation of Turbulent Flows. *J. Phys. Soc. Japan*, 54(8):2834–2839, 1985.

[11] V. Sabelnikov and C. Fureby. LES combustion modeling for high Re flames using a multi-phase analogy. *Combust. Flame*, 160(1):83–96, 2013.

[12] P. J. O'Rourke. *Collective drop effects on vaporizing liquid sprays*. PhD thesis, Los Alamos National Laboratories, Los Alamos, 1981.

[13] R. D. Reitz and R. Diwakar. *Structure of High-Pressure Fuel Sprays*. SAE Technical Paper 870598, 1987.

[14] W. Ranz and W. Marshall. Evaporation from drops. *Chem. Eng. Prog.*, 48:141–146, 1952.

[15] B. Zuo, A. M. Gomes, and C. J. Rutland. Modelling superheated fuel sprays and vaporization. *Int. J. Engine Res.*, 1(4):321–336, 2000.

[16] H. G. Weller, G. Tabor, H. Jasak, and C. Fureby. A tensorial approach to computational continuum mechanics using object-oriented techniques. *Comp. in Physics*, 12:620–631, 1998.

[17] B. Franzelli, E. Riber, M. Sanjosé, and T. Poinsot. A two-step chemical scheme for kerosene–air premixed flames. *Combust. Flame*, 157(7):1364–1373, 2010.

[18] ANSYS Chemkin-Pro. *Ansys, Inc.*, 2016.

[19] N. Zettervall, K. Nordin-Bates, E. J. K. Nilsson, and C. Fureby. Large Eddy Simulation of a premixed bluff body stabilized flame using global and skeletal reaction mechanisms. *Combust. Flame*, 179:1–22, 2017.

[20] K. Kumar, C. Sung, and X. Hui. Laminar flame speeds and extinction limits of conventional and alternative jet fuels. *Fuel*, 90(3):1004–1011, 2011.

[21] C. Liu, R. Zhao, R. Xu, F. N. Egolfopoulos, and H. Wang. Binary diffusion coefficients and non-premixed flames extinction of long-chain alkanes. *Proc. Combust. Inst.*, 36(1):1523–1530, 2017.

[22] S. S Vasu, D. F. Davidson, and R. K. Hanson. Jet fuel ignition delay times: Shock tube experiments over wide conditions and surrogate model predictions. *Combust. Flame*, 152(1):125–143, 2008.

[23] R. W. Bilger. A mixture fraction framework for the theory and modeling of droplets and sprays. *Combust. Flame*, 158:191–202, 2011.